Supplementary Information for "Topological protection of photosynthetic quantum heat engines"

Hang Zhou,[†] Qian-Qian Hong,[†] Xin-Xia Jian,[†] Yan Xing,[‡] Hui Jing,[*,¶] and Chuan-Cun Shu[*,†]

†*Hunan Key Laboratory of Nanophotonics and Devices, Hunan Key Laboratory of Super-Microstructure and Ultrafast Process, and School of Physics, Central South University, Changsha 410083, China*

‡*School of Physics, Zhengzhou University, Zhengzhou 450001, China*

¶*Key Laboratory of Low-Dimensional Quantum Structures and Quantum Control of Ministry of Education, Department of Physics and Synergetic Innovation Center for Quantum Effects and Applications, Hunan Normal University, Changsha 410081, China*

E-mail: jinghui73@foxmail.com; cc.shu@csu.edu.cn

Supplementary Note 1: Lindblad Description of the Photosynthetic Quantum Heat Engine

A. Lindblad model

We consider a four-level photosynthetic quantum heat engine with eigenstates $|0\rangle$, $|1\rangle$, $|2\rangle$, and $|3\rangle$. The states $|3\rangle$ and $|2\rangle$ represent the donor and acceptor excited states, respectively, while $|0\rangle$ and $|1\rangle$ denote the ground and intermediate states involved in the charge-separation cycle. The

system is coherently driven on the donor–acceptor transition between $|3\rangle$ and $|2\rangle$ and interacts with environmental reservoirs that induce excitation, relaxation, and work extraction.

Within the dipole approximation ($\hbar = 1$), the total Hamiltonian can be written as

$$\hat{H} = \hat{H}_S + \hat{H}_V + \hat{H}_B + \hat{H}_{SB}, \tag{1}$$

where $\hat{H}_S = \sum_{i=0}^{3} \omega_i |i\rangle\langle i|$ is the system Hamiltonian with eigenfrequencies ω_i. The coherent donor–acceptor coupling induced by an external field is

$$\hat{H}_V = \Omega \left(e^{i\omega_{32}t} |3\rangle\langle 2| + e^{-i\omega_{32}t} |2\rangle\langle 3| \right), \tag{2}$$

where Ω is the Rabi frequency and $\omega_{32} = \omega_3 - \omega_2$.

The system interacts with radiation and phonon reservoirs modeled as harmonic baths, $\hat{H}_B = \sum_k \nu_k a_k^\dagger a_k$, through dipole-type couplings. Applying the rotating-wave, Born–Markov, and secular approximations to the system–bath interaction yields a Lindblad master equation for the reduced density matrix ρ.

The resulting dynamics of the QHE system are governed by

$$\begin{aligned} \frac{d\rho}{dt} = & -i[\hat{H}_I, \rho] + \Gamma \mathscr{D}[S_{12}] + (n_h + 1)\gamma_h \mathscr{D}[S_{03}] + n_h \gamma_h \mathscr{D}[S_{03}^\dagger] \\ & + (n_c + 1)\gamma_c \mathscr{D}[S_{23}] + n_c \gamma_c \mathscr{D}[S_{23}^\dagger] + (N_c + 1)\Gamma_c \mathscr{D}[S_{01}] + N_c \Gamma_c \mathscr{D}[S_{01}^\dagger], \end{aligned} \tag{3}$$

where $\hat{H}_I = \Omega(|3\rangle\langle 2| + \text{H.c.})$ describes the coherent donor–acceptor interaction and $\mathscr{D}[O]\rho = O\rho O^\dagger - \frac{1}{2}\{O^\dagger O, \rho\}$ is the standard Lindblad dissipator.

The four dissipative channels correspond to the transitions between $|3\rangle$ and $|0\rangle$ (hot-photon bath), $|3\rangle$ and $|2\rangle$ (cold-phonon bath), $|1\rangle$ and $|0\rangle$ (cold relaxation), and $|2\rangle$ and $|1\rangle$ (work extraction). Their associated rates are γ_h, γ_c, Γ_c and Γ respectively. The extraction rate Γ represents the transfer of an electron from the acceptor state to the external load, thereby generating useful work.

The thermal occupation numbers of the reservoirs follow the Bose–Einstein distributions

$$n_h = \frac{1}{e^{\omega_{30}/k_B T_h} - 1}, \qquad n_c = \frac{1}{e^{\omega_{32}/k_B T_c} - 1}, \qquad N_c = \frac{1}{e^{\omega_{10}/k_B T_c} - 1}. \tag{4}$$

For typical ambient conditions with $T_c \approx 300$ K and optical transition energies in the V range, one has $n_c \simeq N_c \simeq 0$.

Equation (3) forms the starting point of our analysis. The coherent interaction $\hat{H}_I$ drives reversible population exchange between the donor and acceptor states, while the dissipative channels govern excitation, relaxation, and energy extraction. The competition between coherent donor–acceptor exchange and environmental decay plays a central role in determining the transport properties and thermodynamic performance of the photosynthetic quantum heat engine.

B. Steady-state solution

From the Lindblad master equation [Eq. (3)], the equations of motion for the relevant density-matrix elements are

$$\begin{aligned}
\dot{\rho}_{33} &= 2i\Omega\rho_{32} - [\gamma_c + \gamma_h(n_h + 1)]\rho_{33} + n_h\gamma_h\rho_{00}, \\
\dot{\rho}_{22} &= -2i\Omega\rho_{32} - \Gamma\rho_{22} + \gamma_c\rho_{33}, \\
\dot{\rho}_{11} &= \Gamma\rho_{22} - \Gamma_c\rho_{11}, \\
\dot{\rho}_{00} &= \Gamma_c\rho_{11} + \gamma_h(n_h + 1)\rho_{33} - n_h\gamma_h\rho_{00}, \\
\dot{\rho}_{32} &= i\Omega(\rho_{33} - \rho_{22}) - \frac{\Gamma + \gamma_c + \gamma_h(n_h + 1)}{2}\rho_{32}.
\end{aligned} \tag{5}$$

Imposing the steady-state condition $\dot{\rho}_{ij} = 0$ yields a closed set of algebraic equations. The population flow between the extraction states $|2\rangle$ and $|1\rangle$ gives the relation

$$\Gamma\rho_{22} = \Gamma_c\rho_{11}, \tag{6}$$

which determines the population balance between the acceptor state and the load relaxation chan-

nel,

$$\rho_{11}(\Omega) = \frac{\Gamma}{\Gamma_c}\rho_{22}(\Omega). \tag{7}$$

Solving the steady-state equations leads to analytical expressions for the density-matrix elements in the coherent subspace,

$$\rho_{33}(\Omega) = \frac{\alpha_1\Gamma^2 + \alpha_2\Gamma + \alpha_3}{\alpha_4\Gamma^2 + \alpha_5\Gamma + \alpha_6}, \qquad \rho_{22}(\Omega) = \frac{\alpha_7\Gamma + \alpha_8}{\alpha_4\Gamma^2 + \alpha_5\Gamma + \alpha_6}, \qquad \rho_{32}(\Omega) = i\frac{\alpha_9\Gamma + \alpha_{10}}{\alpha_4\Gamma^2 + \alpha_5\Gamma + \alpha_6}, \tag{8}$$

The coefficients α_i are

$$\begin{aligned}
\alpha_1 &= \Gamma_c n_h \gamma_h, \\
\alpha_2 &= \Gamma_c n_h \gamma_h (\gamma_c + \gamma_h + n_h\gamma_h), \\
\alpha_3 &= 4\Gamma_c \Omega^2 n_h \gamma_h, \\
\alpha_4 &= \Gamma_c\gamma_c + \Gamma_c\gamma_h + 2\Gamma_c n_h\gamma_h + n_h\gamma_c\gamma_h, \\
\alpha_5 &= 4\Omega^2(n_h\gamma_h + \Gamma_c) + n_h^2\gamma_h^2(\gamma_c + 2\Gamma_c) + n_h(\gamma_c^2\gamma_h + \gamma_c\gamma_h^2 + 4\Gamma_c\gamma_c\gamma_h + 3\Gamma_c\gamma_h^2) + \Gamma_c(\gamma_c + \gamma_h)^2, \\
\alpha_6 &= \Gamma_c\gamma_h(12\Omega^2 n_h + 4\Omega^2 + \gamma_h n_h^2\gamma_c + n_h\gamma_c^2 + \gamma_h n_h\gamma_c), \\
\alpha_7 &= \Gamma_c n_h\gamma_h\gamma_c, \\
\alpha_8 &= \Gamma_c n_h\gamma_h(\gamma_c\gamma_h + 4\Omega^2 + \gamma_c^2 + n_h\gamma_c\gamma_h), \\
\alpha_9 &= 2\Gamma_c\Omega n_h\gamma_h, \\
\alpha_{10} &= -2\Gamma_c\Omega n_h\gamma_h\gamma_c.
\end{aligned} \tag{9}$$

These expressions provide the analytical steady-state populations and coherence as functions of the coherent coupling Ω. In particular, the acceptor population ρ_{22} determines the output current and power of the quantum heat engine in the main text.

C. Voltage, current, and efficiency

In the reaction-center convention commonly used for photosynthetic quantum heat engines, the effective load voltage is defined as the electrochemical potential difference between the acceptor state $|2\rangle$ and the extraction state $|1\rangle$,[1]

$$V \equiv \mu_2 - \mu_1. \tag{10}$$

This definition reflects the work extracted when an electron is transferred from the acceptor to the external circuit.

Assuming local quasi-equilibrium with an auxiliary reservoir at the cold temperature T_c, the steady-state populations follow a grand-canonical distribution

$$p_i \propto \exp\left[-\frac{\omega_i - \mu_i}{k_B T_c}\right]. \tag{11}$$

Taking the ratio of the populations of states $|2\rangle$ and $|1\rangle$ eliminates the normalization factor and gives

$$\frac{\rho_{22}}{\rho_{11}} = \exp\left[-\frac{(\omega_2 - \omega_1) - (\mu_2 - \mu_1)}{k_B T_c}\right]. \tag{12}$$

Substituting $\mu_2 - \mu_1 = V$ yields[2]

$$V = \omega_{21} + k_B T_c \ln\left(\frac{\rho_{22}}{\rho_{11}}\right), \tag{13}$$

which relates the terminal voltage to the population imbalance between the acceptor and extraction states.

Using the steady-state relation $\rho_{11} = (\Gamma/\Gamma_c)\rho_{22}$ derived in Sec. B, Eq. (13) reduces to

$$V = \omega_{21} + k_B T_c \ln\left(\frac{\Gamma_c}{\Gamma}\right). \tag{14}$$

This expression coincides with the detailed-balance condition for the extraction process and shows that the load voltage is determined by the ratio between the extraction rate Γ and the relaxation rate

Γ_c. Solving Eq. (14) for Γ gives

$$\Gamma = \Gamma_c \exp\left[-\frac{V - \omega_{21}}{k_B T_c}\right], \tag{15}$$

which is used in the main text to relate the transport rate to the applied voltage.

The steady-state current flowing through the extraction channel $|2\rangle$ to $|1\rangle$ is defined as

$$j = \Gamma \rho_{22}, \tag{16}$$

and the electrical power delivered to the load is therefore

$$P = V j = \Gamma \rho_{22} V. \tag{17}$$

These quantities characterize the energy flow through the donor–acceptor transport channel established by the coherent coupling.

The thermodynamic efficiency of the heat engine is defined as the ratio of electrical power output to the absorbed photon power per carrier with energy ω_{30},

$$\eta_{\text{th}} = \frac{P}{P_{\text{sun}}} = \frac{V j}{j\omega_{30}} = \frac{V}{\omega_{30}}. \tag{18}$$

This quantity depends only on the output voltage and therefore does not capture the simultaneous changes in power output and conversion performance.

To quantify the operational performance of the device, we introduce a normalized efficiency defined relative to the maximum thermal power supplied by the hot reservoir,

$$\eta = \frac{P}{\eta_C P_{\text{hot}}^{\max}}, \qquad P_{\text{hot}}^{\max} = \omega_{30}\gamma_h n_h, \qquad \eta_C = 1 - \frac{T_c}{T_h}. \tag{19}$$

Here η_C is the Carnot efficiency between the hot and cold reservoirs. The quantity η serves as a dimensionless measure of energy conversion performance, analogous to the power conversion efficiency used in photovoltaic devices, and allows the effects of coherent transport and topological

transitions on both power generation and efficiency to be assessed simultaneously.

D. Analytical Expressions for Current, Power, and Efficiency

The critical Rabi frequency Ω_T obtained in the previous section defines the dynamical scale separating dissipation-dominated and coherence-dominated regimes. When $\Omega < \Omega_T$, the donor–acceptor excitation is rapidly damped by the effective decay channels and the population transfer to the acceptor state remains weak. In contrast, for $\Omega > \Omega_T$ coherent exchange becomes comparable to the effective linewidth, enabling sustained population transfer and enhanced energy conversion. To make this connection explicit, it is convenient to express the steady-state solution obtained in Sec. I in terms of the scale Ω_T.

In deriving the compact analytic expressions below, we use the large-pumping approximation $n_h + 1 \simeq n_h$, valid for $n_h = 10^4$. The relevant density-matrix elements can then be written as

$$\begin{aligned} \rho_{22}(\Omega) &= \frac{\zeta_1\Omega_T^2 + \zeta_2\Omega^2}{\zeta_3\Omega_T^2 + \zeta_4\Omega^2}, \qquad \rho_{33}(\Omega) = \frac{(\Gamma/\gamma_c)\zeta_1\Omega_T^2 + \zeta_2\Omega^2}{\zeta_3\Omega_T^2 + \zeta_4\Omega^2}, \\ \rho_{32}(\Omega) &= \frac{i\,\zeta_5\Omega}{\zeta_3\Omega_T^2 + \zeta_4\Omega^2}, \end{aligned} \tag{20}$$

where the coefficients ζ_i ($i = 1, \ldots, 5$) read

$$\begin{aligned} \zeta_1 &= \Gamma_c\gamma_c n_h\gamma_h(\Gamma + \gamma_c + n_h\gamma_h), \\ \zeta_2 &= \Gamma\Gamma_c n_h\gamma_h(\gamma_c + n_h\gamma_h), \\ \zeta_3 &= (\Gamma + \gamma_c + n_h\gamma_h)[\Gamma\Gamma_c(\gamma_c + 2n_h\gamma_h) + (\Gamma + \Gamma_c)n_h\gamma_c\gamma_h], \\ \zeta_4 &= \Gamma(\gamma_c + n_h\gamma_h)[\Gamma\Gamma_c + n_h\gamma_h(\Gamma + 3\Gamma_c)], \\ \zeta_5 &= \tfrac{1}{2}\Gamma\Gamma_c n_h\gamma_h(\Gamma - \gamma_c)(\gamma_c + n_h\gamma_h). \end{aligned} \tag{21}$$

Substituting ρ_{22} into the definitions of current and power yields the closed-form expressions

$$
\begin{aligned}
j(\Omega) &= \Gamma \frac{\zeta_1 \Omega_T^2 + \zeta_2 \Omega^2}{\zeta_3 \Omega_T^2 + \zeta_4 \Omega^2}, \\
P(\Omega) &= V\Gamma \frac{\zeta_1 \Omega_T^2 + \zeta_2 \Omega^2}{\zeta_3 \Omega_T^2 + \zeta_4 \Omega^2}.
\end{aligned}
\tag{22}
$$

The structure of Eq. (20) reveals that the steady-state populations depend on the coherent coupling Ω only through the competition between the two scales Ω^2 and Ω_T^2. The critical scale $\Omega_T = \sqrt{\Gamma\Gamma_{\text{eff}}}/2$ therefore marks the point where coherent donor–acceptor exchange becomes comparable to the effective dissipative linewidth. For $\Omega \ll \Omega_T$, the denominators in Eq. (20) are dominated by Ω_T^2, and the dynamics are controlled by dissipative relaxation processes. In this regime the population injected into the donor state rapidly decays before coherent exchange can efficiently transfer excitation to the acceptor. As a result, the acceptor population ρ_{22} and the associated current remain small.

In contrast, when Ω approaches and exceeds Ω_T, the coherent exchange term Ω^2 becomes comparable to the dissipative scale Ω_T^2. This crossover enables sustained excitation exchange between the donor and acceptor states, stabilizing the population flow into the extraction channel. Consequently, ρ_{22} increases and the electrical current $j = \Gamma\rho_{22}$ grows, producing the coherence-assisted power enhancement discussed in the main text.

Supplementary Figure 1 illustrates the dependence of output power and thermodynamic efficiency on the terminal voltage. The power curves compare two regimes: the incoherent limit $\Omega = 0$ and the coherence-assisted case $\Omega = \Omega_T(V)$. While the thermodynamic efficiency $\eta_{\text{th}} = V/\omega_{30}$ increases linearly with V, the electrical power exhibits a pronounced maximum within the voltage interval $0.90\,\omega_{21} \lesssim V \lesssim \omega_{21}$. This region defines the operating window where both finite power output and coherent donor–acceptor exchange are possible.

The lower bound of this interval arises from the rapid growth of the extraction rate Γ at small voltages. Since $\Omega_T = \sqrt{\Gamma\Gamma_{\text{eff}}}/2$, a large Γ drives the critical Rabi frequency far above the accessible driving range, preventing the formation of coherent donor–acceptor oscillations. For V sufficiently

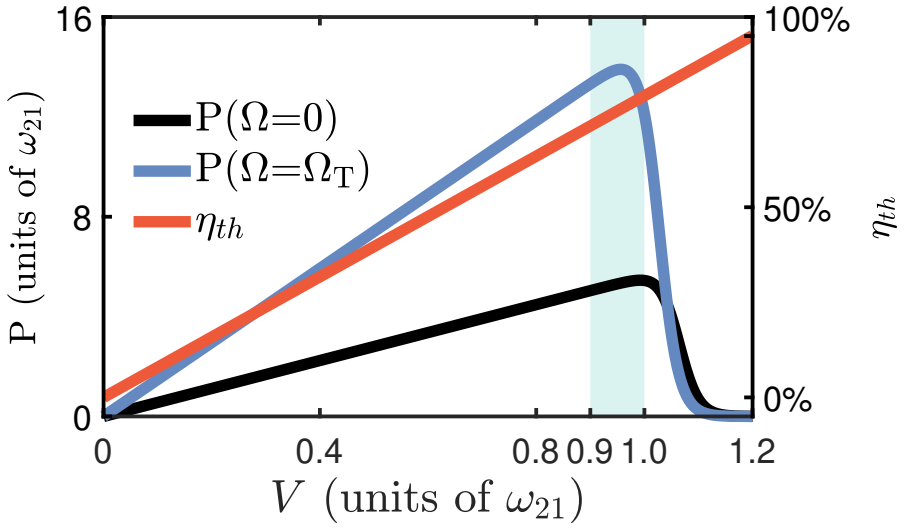

Supplementary Figure 1: Output power P (left axis) and thermodynamic efficiency η_{th} (right axis) as functions of the terminal voltage V. The black and blue curves show the power P for $\Omega = 0$ and $\Omega = \Omega_T(V)$ respectively. The thermodynamic efficiency $\eta_{\text{th}} = V/\omega_{30}$ is plotted for reference on the right axis.

above ω_{21}, detailed balance forces $\Gamma \to 0$, interrupting the population flow from $|2\rangle$ to $|1\rangle$ and causing the output power to collapse even though η_{th} continues to grow.

To quantify the performance enhancement associated with coherence, we introduce the normalized efficiency

$$\eta = \frac{\Gamma_c V}{\eta_C \omega_{30} \gamma_h n_h} \exp\left[-\frac{V-\omega_{21}}{k_B T_c}\right] \frac{\zeta_1 \Omega_T^2 + \zeta_2 \Omega^2}{\zeta_3 \Omega_T^2 + \zeta_4 \Omega^2}, \tag{23}$$

which explicitly incorporates the coherence-enhanced population transfer.

The donor–acceptor coherence provides further insight into this transition. The ℓ_1-norm coherence $C_{\ell_1} = 2|\rho_{32}|$ characterizes the magnitude of the off-diagonal element of the density matrix and therefore measures the strength of coherent superposition between the two levels. As Ω increases from zero, C_{ℓ_1} grows rapidly because coherent coupling begins to compete with the dissipative decay channels. However, once the system enters the coherence-dominated regime, the population exchange becomes dynamically stabilized and the coherence amplitude no longer needs to increase. Instead, the coherent transport rate $J_c = \Omega C_{\ell_1}$ continues to rise and eventually saturates, indicating the formation of a stable energy-transfer channel between the donor and acceptor states.

The ℓ_1-norm coherence between donor and acceptor states is given by

$$C_{\ell_1} = 2|\rho_{32}| = \frac{2\zeta_5\Omega}{\zeta_3\Omega_T^2 + \zeta_4\Omega^2}, \tag{24}$$

reaching its extremum at

$$\Omega_c^{\mathrm{coh}} = \sqrt{\frac{\zeta_3}{\zeta_4}}\Omega_T. \tag{25}$$

The associated energy transfer rate $J_c = \Omega C_{\ell_1}$ is directly related to the efficiency enhancement shown in the main text.

Although $\eta(\Omega)$ increases smoothly as Ω grows, the precise location of the transition can be identified from the curvature of the efficiency. The Hessian reads

$$\frac{d^2\eta}{d\Omega^2} = \frac{2\Gamma V\Omega_T^2(\zeta_2\zeta_3 - \zeta_1\zeta_4)(\zeta_3\Omega_T^2 - 3\zeta_4\Omega^2)}{\omega_{30}n_h\gamma_h\eta_C(\zeta_3\Omega_T^2 + \zeta_4\Omega^2)^3}, \tag{26}$$

whose minimum occurs at

$$\Omega_c^{\mathrm{Hessian}} = \sqrt{\frac{\zeta_3}{\zeta_4}}\Omega_T. \tag{27}$$

The coincidence between the coherence extremum Ω_c^{coh} and the Hessian minimum $\Omega_c^{\mathrm{Hessian}}$ reveals that the same dynamical scale governs the maximum coherent transfer and the most rapid change in efficiency. This characteristic scale $\Omega_c = \sqrt{\zeta_3/\zeta_4}\,\Omega_T$ therefore provides an operational signature of the underlying topological transition. While the winding number introduced in Sec. II B identifies the transition at the level of the spectral response, the coherence peak and the efficiency curvature offer experimentally accessible indicators of the same transition in the observable transport properties of the quantum heat engine.

Supplementary Note 2: Numerical Validation and Dynamical Properties

A. Feedback-induced renormalization of the critical Rabi frequency

The two-level non-Hermitian reduction retains only the coherent dynamics in the subspace $\{|3\rangle, |2\rangle\}$, while the incoherent processes are incorporated into the effective decay scales entering the diagonal elements of $\hat{H}_c$. In this reduced description, the donor state $|3\rangle$ is characterized by the linewidth Γ_{eff}, whereas the acceptor state $|2\rangle$ is depleted by the extraction rate Γ. This reduction is accurate only when population leaving the coherent manifold through the auxiliary states does not return on comparable timescales.

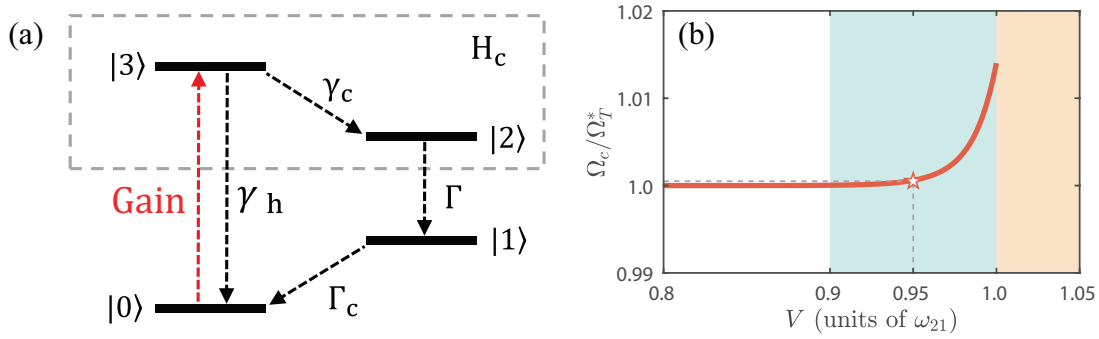

Supplementary Figure 2: Renormalized critical Rabi frequency in the reduced two-level description. (a) Schematic illustration of the coherent subspace governed by $\hat{H}_c$ and the auxiliary recycling pathway involving the states $|1\rangle$ and $|0\rangle$. The red dashed arrow denotes the feedback-induced reinjection channel associated with population recycling. (b) Ratio Ω_c/Ω_T^* extracted from the full Lindblad dynamics as a function of the terminal bias V (in units of ω_{21}). The cyan-shaded region indicates the bias window where the engine delivers finite power, while the yellow region marks the onset of the limiting operating regime. The star marks the operating point used in Fig. 2 of the main text.

Supplementary Figure 2(a) illustrates how this assumption is modified in the full four-level engine. Besides the direct decay channels associated with γ_c and the hot-bath processes, the extraction pathway $|3\rangle \rightarrow |2\rangle \rightarrow |1\rangle \rightarrow |0\rangle$ forms a closed recycling loop once the hot reservoir repopulates $|3\rangle$. In the reduced description, this loop acts as an effective feedback channel: a fraction of the probability current that leaves the coherent manifold through extraction is reinjected

into the donor state, thereby renormalizing the effective linewidth that enters $\hat{H}_c$. The red arrow in Supplementary Fig. 2(a) schematically represents this feedback-induced correction to the loss budget. We therefore parameterize the renormalized donor linewidth in the multiplicative form

$$\Gamma^*_{\mathrm{eff}}(\Gamma) = \alpha(\Gamma)\,\Gamma_{\mathrm{eff}}, \tag{28}$$

where the dimensionless factor $\alpha(\Gamma)$ encodes the net balance between irreversible loss and recycling-induced reinjection.

To obtain a minimal analytic form for $\alpha(\Gamma)$, we denote by $W_h \equiv n_h\gamma_h$ the hot-induced transition rate associated with repopulation from $|0\rangle$ to $|3\rangle$. Since the auxiliary states $\{|1\rangle, |0\rangle\}$ enter linearly and couple to the coherent subspace only through irreversible transitions, their elimination generates a self-energy correction to the effective propagator of $\{|3\rangle, |2\rangle\}$. Because the auxiliary sector is governed predominantly by the single relaxation scale $\Gamma_c + W_h$, the leading feedback correction is naturally captured by a single-pole rational approximation in the extraction rate Γ. We therefore model $\alpha(\Gamma)$ by the lowest-order Padé form whose numerator and denominator are linear in Γ.

To incorporate the effect of the recycling pathway into the reduced two-level description, we introduce a feedback-induced multiplicative renormalization of the coherent-subspace linewidth, $\Gamma^*_{\mathrm{eff}}(\Gamma) = \alpha(\Gamma)\Gamma_{\mathrm{eff}}$. Here Γ_{eff} denotes the bare linewidth entering the reduced non-Hermitian Hamiltonian, whereas $\alpha(\Gamma)$ accounts for the modification of the effective dissipation kernel induced by the auxiliary pathway $|2\rangle \to |1\rangle \to |0\rangle \to |3\rangle$. The rational form of $\alpha(\Gamma)$ is chosen as a minimal Padé-type closure constrained by the limiting response of the full four-level dynamics.

In the weak-extraction limit, $\Gamma \to 0$, the recycling current through the auxiliary manifold is suppressed. The feedback channel then produces only a symmetric low-frequency dressing of the bare coherent-subspace linewidth, giving $\Gamma^{*(0)}_{\mathrm{eff}} = \lim_{\Gamma\to 0}\Gamma^*_{\mathrm{eff}}(\Gamma) = \Gamma_{\mathrm{eff}}/2$. In the rapid-extraction limit, $\Gamma \to \infty$, population is rapidly transferred through the auxiliary manifold before intrinsic relaxation can equilibrate the coherent subspace. The feedback kernel then approaches a saturated loss budget governed by the auxiliary relaxation bandwidth $\Gamma_c + W_h$, yielding $\Gamma^{*(\infty)}_{\mathrm{eff}} =$

$\lim_{\Gamma\to\infty}\Gamma^{*}_{\mathrm{eff}}(\Gamma) = (3\Gamma_c + W_h)\Gamma_{\mathrm{eff}}/2/(\Gamma_c + W_h)$, where $W_h = n_h\gamma_h$ denotes the hot-induced repumping rate. The crossover between these limits is controlled by the competition between the extraction rate Γ and the hot-repumping bottleneck W_h. This motivates the dimensionless interpolation factor

$$\alpha(\Gamma) = \frac{(3\Gamma_c + W_h)\Gamma + W_h(\Gamma_c + W_h)}{2(\Gamma + W_h)(\Gamma_c + W_h)}. \tag{29}$$

By construction, $\lim_{\Gamma\to 0}\alpha(\Gamma) = 1/2$, and $\lim_{\Gamma\to\infty}\alpha(\Gamma) = (3\Gamma_c + W_h)/2/(\Gamma_c + W_h)$, so that the renormalized linewidth $\Gamma^{*}_{\mathrm{eff}}(\Gamma) = \alpha(\Gamma)\Gamma_{\mathrm{eff}}$ remains finite in both extraction limits.

Substituting $\Gamma^{*}_{\mathrm{eff}} = \alpha(\Gamma)\Gamma_{\mathrm{eff}}$ into the non-Hermitian threshold condition yields the feedback-renormalized critical Rabi frequency

$$\Omega^{*}_{T} = \frac{1}{2}\sqrt{\Gamma\,\Gamma^{*}_{\mathrm{eff}}}. \tag{30}$$

The scale Ω^{*}_{T} therefore incorporates the feedback-induced dressing of the dissipation kernel while preserving the analytic structure of the reduced two-level description.

Supplementary Figure 2(b) displays the ratio Ω_c/Ω^{*}_{T} extracted from the full Lindblad dynamics as a function of the terminal bias V. The cyan-shaded region marks the operational window where the engine delivers finite power, while the yellow region indicates the onset of the limiting regime. Over most of the power-producing window, the ratio remains close to unity, demonstrating that the multiplicative renormalization $\Gamma^{*}_{\mathrm{eff}} = \alpha(\Gamma)\Gamma_{\mathrm{eff}}$ captures the dominant feedback correction to the non-Hermitian threshold. As V approaches the upper edge of the operational window, Ω_c/Ω^{*}_{T} gradually deviates from unity, signaling the breakdown of the minimal single-pole Padé approximation. Physically, increasing V suppresses the extraction rate and lengthens the residence time in the auxiliary manifold, thereby weakening the effectiveness of recycling-induced feedback. In this regime, the coherent subspace becomes progressively more sensitive to the bare extraction loss, and higher-order dynamical corrections beyond the minimal renormalization become relevant. The systematic trend observed in Supplementary Fig. 2(b) therefore confirms that Ω^{*}_{T} provides a quantitatively accurate and physically transparent estimate of the critical drive over the experimentally

relevant bias window, while also clarifying the parameter range in which the reduced two-level description remains reliable.

B. Exceptional Point and Its Separation from the TPT Mechanism

To further clarify that the TPT is not associated with an exceptional point (EP), we explicitly analyze the reduced non-Hermitian Hamiltonian of the coherent subspace,

$$\hat{H}_c = \begin{pmatrix} -\frac{i}{2}\Gamma_{\rm eff} & \Omega \\ \Omega & -\frac{i}{2}\Gamma \end{pmatrix}, \qquad \Gamma_{\rm eff} = \gamma_h(n_h+1) + \gamma_c, \tag{31}$$

whose eigenvalues are

$$\lambda_\pm = \frac{-i(\Gamma_{\rm eff}+\Gamma)}{4} \pm \frac{1}{4}\sqrt{16\Omega^2 - (\Gamma_{\rm eff}-\Gamma)^2}\,. \tag{32}$$

The EP corresponds to the branch-point degeneracy where the discriminant vanishes, leading to

$$\Omega_{\rm EP} = \frac{|\Gamma_{\rm eff}-\Gamma|}{4} = \frac{|\Gamma_{\rm eff}-\Gamma|}{2\sqrt{\Gamma\Gamma_{\rm eff}}}\,\Omega_T, \qquad \Omega_T = \sqrt{\frac{\Gamma\Gamma_{\rm eff}}{2}}. \tag{33}$$

By contrast, the TPT is characterized by the critical Rabi frequency $\Omega_c = \sqrt{\zeta_3/\zeta_4}\,\Omega_T$, extracted simultaneously from the maximum of the donor–acceptor coherence and from the Hessian minimum of the efficiency. This critical point is determined solely by the competition between coherent transfer and residual dissipation, and therefore does not rely on spectral coalescence or non-Hermitian degeneracy.

Supplementary Figure 3 shows the ratio $\Omega_{\rm EP}/\Omega_c$ as a function of the terminal voltage V. When $V < 0.90\omega_{21}$, Ω_c remains much smaller than $\Omega_{\rm EP}$, indicating that the coherent-subspace dynamics lies deep in the broken phase. At $V = 0.956\omega_{21}$, the two scales become equal, marking the crossover point where Ω_c enters the unbroken regime. As V increases further, Ω_c continues to grow and exceeds $\Omega_{\rm EP}$, while $\Omega_{\rm EP}/\Omega_c$ rapidly decreases when V approaches ω_{21}. This separation

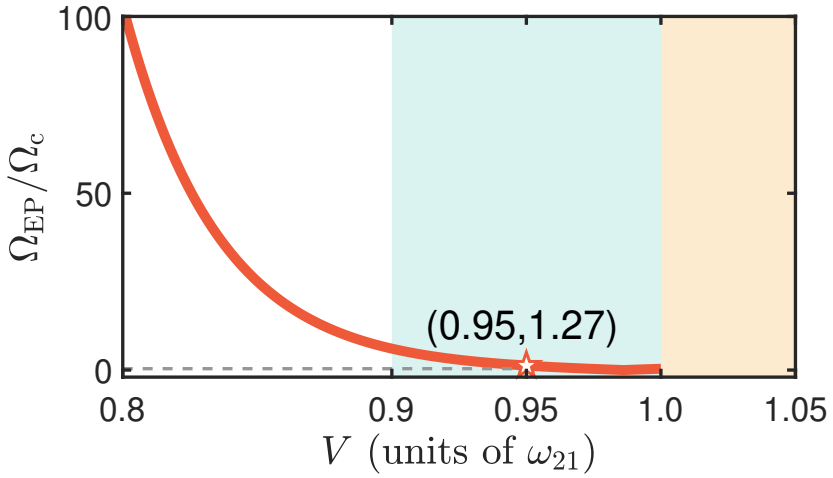

Supplementary Figure 3: Ratio $\Omega_{\mathrm{EP}}/\Omega_c$ as a function of the load voltage V (in units of ω_{21}). The red solid curve displays the voltage dependence of $\Omega_{\mathrm{EP}}/\Omega_c$, with the red star marking the operating point used in the main analysis. The cyan-shaded region denotes the finite-power operating window, while the yellow region indicates the limiting regime where energy extraction is suppressed. The vertical dashed line corresponds to $V = 0.95\,\omega_{21}$.

demonstrates that the onset of maximal coherence is not associated with the spectral singularity of $\hat{H}_c$ but originates from a distinct mechanism: the topological change of the Laplace-domain winding number. Therefore, the TPT characterizes a global transition in the analytic structure of the coherent propagator and remains outside the conventional framework of exceptional-point physics. Such spectral separation ensures that topological protection arises not from mode coalescence but from the intrinsic stabilization of energy transfer, revealing a fundamentally different mechanism from previously reported EP-driven behaviors in non-Hermitian systems.

C. Transient Dynamics of Populations and Coherence

This subsection examines how the four-level quantum heat engine approaches its steady state by solving the time-dependent Lindblad master equation for representative driving strengths below, near, and above the critical value Ω_T. Supplementary Figure 4 tracks the temporal evolution of the populations, the population imbalance $\rho_{33}(t) - \rho_{22}(t)$, and the ℓ_1-norm coherence C_{ℓ_1}. In the weak-driving regime, the donor and acceptor populations relax smoothly toward their stationary values without sustained oscillations, indicating that the dynamics remain predominantly

dissipation-dominated. As the drive is increased toward Ω_T, the transient coherence develops a more pronounced peak, showing that coherent exchange becomes increasingly important during the relaxation process. At stronger driving, the acceptor population rises more rapidly and reaches a larger stationary value, while the ground-state population is depleted accordingly. The time-domain results therefore reveal a clear crossover in the relaxation dynamics as the system is tuned across the critical scale. More importantly, the transient dynamics provide a time-resolved coun-

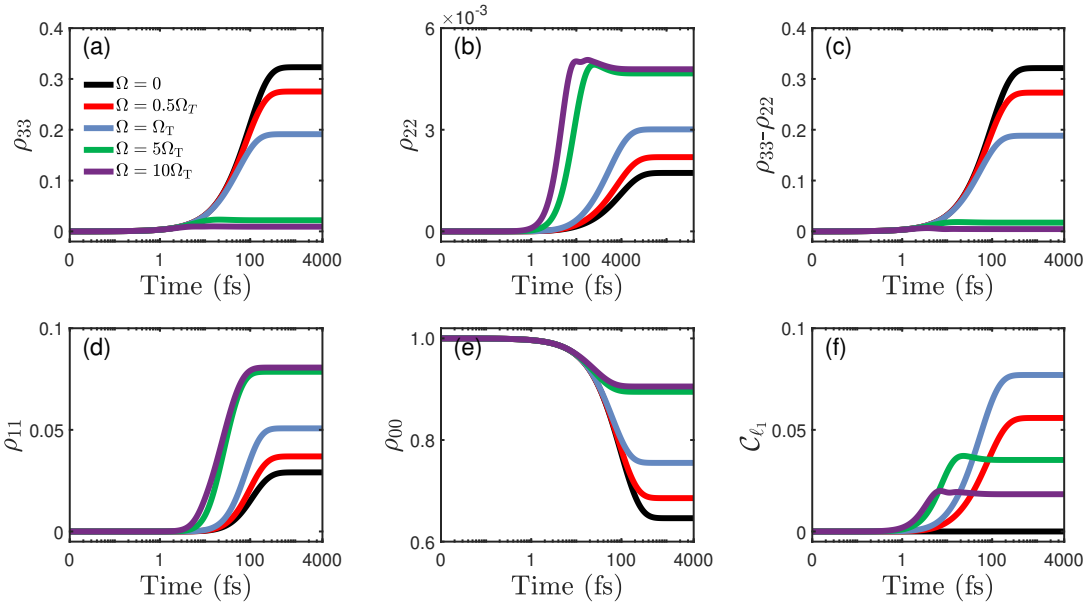

Supplementary Figure 4: (a) Donor population $\rho_{33}(t)$, (b) acceptor population $\rho_{22}(t)$, (c) population difference $\rho_{33}(t) - \rho_{22}(t)$, (d) ionized-state population $\rho_{11}(t)$, (e) ground-state population $\rho_{00}(t)$, and (f) ℓ_1-norm coherence C_{ℓ_1}, for $\Omega = 0$ (black), $0.5\Omega_T$ (red), Ω_T (blue), $5\Omega_T$ (green), and $10\Omega_T$ (purple). The logarithmic time axis highlights both the ultrafast coherent oscillations and long-time relaxation dynamics.

terpart to the steady-state topological picture established in the main text. Near and above Ω_T, the population difference $\rho_{33} - \rho_{22}$ is strongly reduced, indicating that the donor and acceptor states evolve toward an increasingly symmetric occupation pattern. At the same time, the coherence reaches its largest transient response near the transition, but does not continue to grow indefinitely at larger Ω, consistent with the steady-state result that maximal transport performance does not require maximal coherence amplitude. Instead, the strong-driving regime is characterized by

the formation of a stable and nearly balanced donor–acceptor manifold, which supports efficient population transfer while suppressing further dynamical restructuring. In this sense, the transient evolution confirms that the topological transition is not only encoded in spectral and steady-state observables, but also manifests itself as a qualitative reorganization of the relaxation pathway toward the symmetry-stabilized transport regime.

D. Optimal Observation of Topological Enhancement Regime

To examine how driving strength shapes steady-state performance at various load voltages, we analyze the efficiency and coherence of the four-level QHE across a wide range of Rabi frequencies. Supplementary Figure 5 presents the normalized efficiency η, Hessian function $\mathcal{H}_\eta$, coherence C_{ℓ_1}, and coherent transfer rate J_c as functions of the Rabi frequency Ω for four representative voltages: $V = 0.94\,\omega_{21}$, $0.96\,\omega_{21}$, $0.98\,\omega_{21}$, and $1.0\,\omega_{21}$. For each voltage, the left vertical axis shows either η or C_{ℓ_1}, while the right axis displays the corresponding $\mathcal{H}_\eta$ or J_c. Vertical dashed lines mark the critical Rabi frequency Ω_T for each V, and shaded regions denote the trivial and nontrivial phase regimes.

Supplementary Figure 5 illustrates how load voltage and coherent driving jointly determine the critical Rabi frequency Ω_T. As load voltage V increases from $0.94\omega_{21}$ to $1.0\omega_{21}$, the relaxation rate Γ decreases, shifting Ω_T toward weaker driving strengths, as indicated by the vertical dashed lines moving left from panels (a) to (d). At $V = 0.94\omega_{21}$, Ω_T occurs at a comparatively larger Ω, and the efficiency η increases smoothly across the transition while the ℓ_1-norm coherence C_{ℓ_1} exhibits a distinct peak near Ω_T; correspondingly, the coherent transfer rate J_c rises rapidly and then approaches a plateau as Ω increases. When V is increased to $0.96\omega_{21}$ and $0.98\omega_{21}$, the left-shifted Ω_T is accompanied by a sharper coherence peak around Ω_T, while η displays a faster crossover toward its high-Ω plateau, and J_c again quickly saturates after the transition. At the higher voltage $V = 1.0\omega_{21}$, Ω_T moves further to the low-Ω side and the coherence peak becomes more pronounced.

The interplay among η, C_{ℓ_1}, and J_c shows that significant enhancement occurs only within a

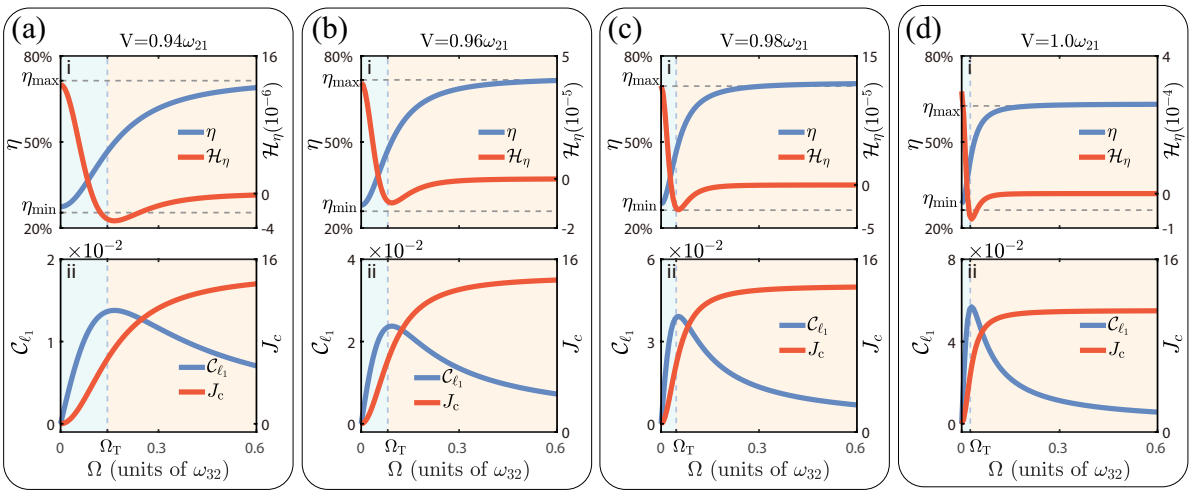

Supplementary Figure 5: Performance and coherence characteristics as functions of the Rabi frequency Ω for four load voltages $V = 0.94\,\omega_{21}$, $0.96\,\omega_{21}$, $0.98\,\omega_{21}$, and $1.0\,\omega_{21}$. For each voltage, the upper panels show the normalized efficiency η (left axis) and the Hessian function $\mathcal{H}_\eta$ (right axis), while the lower panels display the ℓ_1-norm coherence C_{ℓ_1} (left axis) and the coherent transfer rate J_c (right axis). Vertical dashed lines indicate the corresponding critical Rabi frequency Ω_T, and the shaded regions delineate the driving regimes on either side of this point.

narrow voltage range, avoiding excessive dissipation at low V and extraction bottlenecks at high V. Supplementary Figure 1 demonstrates that output power peaks near $V \simeq 0.95\omega_{21}$. At this voltage, the critical Rabi frequency is accessible, and the extraction pathway remains conductive enough to enable efficient coherent transfer. Thus, $V = 0.95\omega_{21}$ is identified as the optimal operating point and is used as the representative value in the main text.

Supplementary References

(1) Scully, M. O. Quantum Photocell: Using Quantum Coherence to Reduce Radiative Recombination and Increase Efficiency. *Phys. Rev. Lett.* **2010**, *104*, 207701.

(2) Dorfman, K. E.; Voronine, D. V.; Mukamel, S.; Scully, M. O. Photosynthetic reaction center as a quantum heat engine. *Proc. Natl. Acad. Sci. U.S.A.* **2013**, *110*, 2746–2751.